Romain Gers[1,2,3]
Dominique Anne-Archard[1,3]
Eric Climent[1,3]
Dominique Legendre[1,3]
Christine Frances[2,3]

[1] Université de Toulouse, INPT, UPS, IMFT (Institut de Mécanique des Fluides de Toulouse), Toulouse, France.

[2] Université de Toulouse, INP, UPS, LGC (Laboratoire de Génie Chimique), Toulouse, France.

[3] CNRS, Fédération de Recherche FERMAT, Toulouse, France.

Research Article

Two Colliding Grinding Beads: Experimental Flow Fields and Particle Capture Efficiency

Hydrodynamics plays a major role in wet grinding processes used to produce nanoparticles, but its influence on the mechanisms of fragmentation is not fully understood. The focus is on hydrodynamics in the gap between two grinding beads. Using particle image velocimetry in a large-scale experiment, the velocity field between the beads has been investigated when the beads get closer (down to one-tenth of their radius). Different configurations have been studied, varying from frontal approach to tangential collision. Finally, a capture probability of suspended particles has been estimated.

Keywords: Hydrodynamics, Particle processing, Velocity distribution, Wet milling

Received: April 7, 2010; *revised:* July 6, 2010; *accepted:* July 6, 2010

DOI: 10.1002/ceat.201000156

1 Introduction

During the last decade, it has been recognized that stirred media milling is an effective process to produce nanoparticles in concentrated suspensions, especially for insoluble or poorly soluble products in water [1–3]. However, the physical mechanisms leading to fragmentation in such devices are not fully understood and the grinding process remains laborious because of the large amount of mechanical energy needed. Many experiments have shown that the particle size reaches a steady distribution during the fragmentation process [4]. So, it is important to achieve a basic knowledge of the grinding mechanisms for predicting the minimum particle size for prescribed operating conditions. The high level of energy consumption also induces grinding media wear and a possible contamination of the product. Additional difficulties arise since it is necessary to prevent aggregation within the ground suspension depending on the solid and fluid phases considered. Another limiting factor is related to the hydrodynamics inside the grinding chamber. The hydrodynamics is concerned with two very different length scales: the mill dimensions and the beads' diameter. On the one hand, the grinding chamber and the agitator, depending on their specific geometries, induce complex motion of the beads and the suspension inside the chamber. On the other hand, the beads lead to the fragmentation of the particles suspended in the carrying fluid as a result of their capture and stress during the beads' collision. The geometric collision configuration and its intensity depend on many parameters: geometries of the grinding chamber and agitator, stirrer rotation rate, size, density, and filling ratio of the grinding beads. When two grinding beads collide, they induce fluid motion in the gap between their solid surfaces. But, only particles remaining in the active volume between the beads may likely be crushed. Moreover, when the beads approach, the fluid drainage modifies the energy available to stress the particles. Actually, hydrodynamic interactions between the grinding beads lead to a significant reduction of the energy transferred to particles.

Several studies have been reported in the literature characterizing the global hydrodynamics inside the grinding chamber of media mills. Most of these analyses have been carried out numerically, by Eulerian modeling [5, 6] or by discrete element method simulations [7–10]. Very few experimental studies using particle tracking velocimetry are available. They focused on investigating the fluid motion assuming that the system was equivalent to a one-phase fluid. They were aiming at estimating the bead velocities in the regions located between the agitator disks and inside the gap between the disks and the chamber wall [11, 12]. Moreover, Kwade [13] theoretically expressed and compared the energies available to break the particles during the bead collisions depending on various mechanisms. His analysis revealed that the bead collisions in a plane parallel to the disks were mainly responsible for particle fragmentation.

However, we are not aware of any numerical simulation analyzing locally the mechanism of particle capture during the collision of grinding beads. An experimental attempt was done by Mende [14] who considered a model apparatus with a magnification factor of 100 compared to the real stirred media mill. In this experiment, a grinding ball was moved by a stepper motor either towards a smooth wall or towards another fixed grinding ball. Concerning the number of particles cap-

Correspondence: Dr. C. Frances (Christine.Frances@ensiacet.fr), Laboratoire de Génie Chimique, UMR CNRS 5503, 4 Allée Emile Monso, BP 84234, F-31432 Toulouse Cedex 4, France.

tured during a bead collision, it was concluded that it does not depend on the bead velocity (for a bead Reynolds number varying from 500 to 2500) because of the existence of a tangential flow sweeping the bead surface. Beyond the specific literature on grinding, works focused on the collision between two spheres usually summarize the dynamics by means of two dimensionless numbers: the Stokes number and the restitution coefficient. These works point out a critical Stokes number beyond which the bead rebounds after the collision [15–18].

It is aimed to give more insight into the hydrodynamic limitations in the size reduction process occurring during stirred media milling. Predicting the efficiency of a collision between two grinding beads and the number of captured and broken particles during one single collision could help optimizing the mill process. Due to the bead size and solid load in the mill, it is unrealistic to get this information directly in situ. Only an experimental model focusing on two isolated grinding beads would allow analyzing the fluid drainage by the approach of the two solid surfaces. Thus, the motion of the particles could be analyzed as function of the beads' approaching velocity, the nature of the carrying fluid, or the relative orientation of the beads before their impact.

2 Configuration of Approaching Beads and Experimental Technique

2.1 Practical Information for the Design of the Experimental Device

Our study is based on the measurement of the fluid flow between two approaching beads. To achieve this information with classical optical techniques, the size of the beads compared to the actual dimension related to a stirred media mill has to be enlarged. The model device was built based on a similarity analysis. First the Reynolds number is considered, characteristic of the hydrodynamic phenomena when two grinding beads collide, respectively in the stirred mill and in the model apparatus. The similarity condition in Reynolds writes in the following way:

$$\frac{D_b \Delta U}{\nu_s} = \frac{D_s V_a}{\nu_s^*} \quad (1)$$

where D_b is the grinding media diameter, ΔU is the maximum relative velocity when two beads approach each other in the mill, ν_s is the kinematic viscosity of the suspension to be ground, D_s is the sphere diameter in the experimental device, V_a is the approach velocity in the experimental device, and ν_f is the kinematic viscosity of the fluid chosen for the experiments. An additional criterion to choose the spheres' diameter is the ratio between the beads' size and the product particle size. Considering that the tracer particles used for particle image velocimetry (PIV) stand for the particles to be ground, spheres with a diameter around 60 mm were chosen.

One important parameter is the approach velocity V_a. The velocity range was chosen, considering the relative speed ΔU of colliding beads in the stirred mill. The typical range of variation of this quantity was deduced from a former numerical analysis [19] in which the hydrodynamics inside the grinding chamber of a stirred media mill was investigated. In this work, the flow was simulated by direct numerical solution of the Navier-Stokes equations for an equivalent fluid. The viscosity of the equivalent fluid, representing the complex system composed by the grinding beads, the particles, and the carrying fluid, was modeled by a Krieger-Dougherty law. Depending on the Reynolds number and the non-Newtonian behavior of the fluid, it was observed that several secondary vortices are formed in the plane perpendicular to the main azimuthal flow. The most energetic collisions are driven by a strong shear experienced by the suspension within the gap between the disc tip and the chamber wall. Collision velocities were then estimated from the flow fields. Maximum relative velocities were obtained by computing the eigenvalues of the deformation rate tensor. In agreement with other studies [13], collisions induced by a strong shear in the disc plane were shown which were the most intense and efficient ones for the fragmentation of particles. However, the corresponding maximum velocities reach not more than 10 % of the tangential velocity at the disc tip. The simulations also predicted low impact Stokes numbers indicating no bead rebound after the collision.

Using these previous results, an experimental device was built. A schematic diagram is presented in Fig. 1. The spheres (radius $R = D_s/2$) representing the colliding beads are embedded in a fluid contained in a rectangular vessel. The bottom sphere is fixed while the top sphere is moved in a rectilinear motion by means of a high-precision stepper motor which controls speed and the initial and final positions. Starting from the fluid at rest and with an initial distance between spheres larger than $8R$, a sequence consists in moving the top sphere towards the fixed one at a given velocity V_a (see Fig. 2), in a frontal (along the center line) or oblique way (off-centered). Based on the similarity analysis, the velocity V_a was chosen in

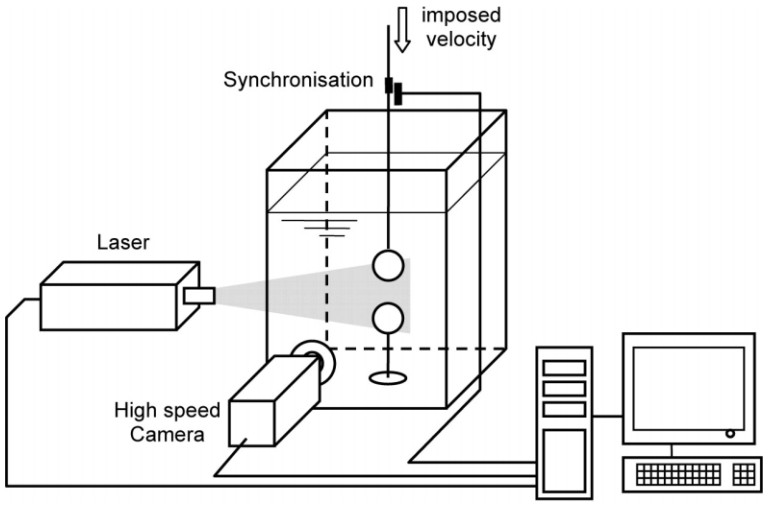

Figure 1. Scheme of the experimental device.

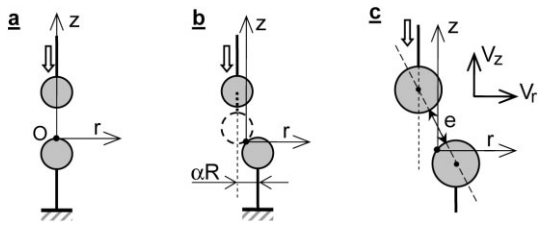

Figure 2. Schematic view of both configurations;. (a) Frontal approach ($\alpha = 0$), (b) oblique approach ($0 < \alpha \leq 2$), (c) distance between spheres.

the range of 1 to 10 mm s^{-1}. The moving sphere was stopped before it actually touches the fixed one. The minimum distance between the two solid surfaces is $6 \cdot 10^{-3}$ R. PIV measurements were obtained in a vertical plane crossing the spheres by their centers (in the plane of symmetry for oblique approach).

The colliding beads were made of crystal (diameter 56 mm for frontal collision) or polystyrene (diameter 60 mm for oblique collision). The fixed sphere was located at 150 mm ($5R$) from the bottom of the tank. This distance, as well as the dimensions of the tank (inner section 240×240 mm^2, height 600 mm), were selected to minimize hydrodynamic interactions with the walls.

The two configurations, i.e., frontal and oblique approaches, and the set of axes used are presented in Fig. 2. Note that the origin is chosen at the contact point on the fixed sphere. The oblique approach is defined through the parameter α, αR being the distance between the direction of motion and the center of the fixed sphere. The position of the moving sphere is defined by the distance e between the spheres (Fig. 2c).

The fluid used was water for the Newtonian case and xanthan solution for the non-Newtonian experiments. In order to quantitatively measure the velocity fields by PIV techniques, the fluid was seeded with PS particles (1 to 20 µm) with encapsulated rhodamine B. As the density of these particles is nearly 1.05, the fluid density was matched to the tracer density by adding NaCl at a concentration of 80 g L^{-1} to prevent settling. A nonionic surfactant (Triton X-100) was added to ensure a correct dispersion of particles.

Some experiments were done using shear-thinning fluids to take into account the non-Newtonian behavior of the fluid around grinding beads in the mill (water + additives + particles to be crushed) [20]. Two xanthan solutions (Satiaxane CX 910, Degussa Texturant Systems) with mass concentrations of 330 and 500 ppm were used to obtain a shear-thinning behavior similar to those observed in real cases. The apparent viscosity of the solutions was measured using a Bohlin C-VOR rheometer. The shear viscosity data were found to be well characterized by a power-law model: $\mu_f = K\dot{\gamma}^{n-1}$. The consistency parameter K was equal to, respectively, 0.0164 Pa s^n and 0.0395 Pa s^n and the power-law index n was equal to 0.68 and 0.58.

Results are presented in dimensionless scaling distances by the sphere radius R and velocities by the approaching velocity V_a. Current research is focused on the fluid drainage within the gap defined by the two solid surfaces. Therefore, the appropriate Reynolds number for such a flow is based on the approaching velocity V_a and the distance between the two grinding beads e, together with the kinematic viscosity of the fluid ν_f:

$$\mathrm{Re} = \frac{V_a\, e}{\nu_f} \tag{2}$$

2.2 Experimental Techniques

The PIV system consists of a laser source, a high-speed camera with a synchronizing timing hub, and a personal computer for data acquisition. The planar laser sheet was generated by a monochromatic Nd:YLF source (Pegasus, 2 × 10 mJ at 1 kHz, 527 nm, New Wave Research). It was adjusted to be perpendicular to one wall of the rectangular tank leading to an illumination of a vertical plane containing the sphere centers. The thickness of the laser sheet is around 500 µm. The fluorescent rhodamine-B compound of seeding particles re-emits light in a spectral range from 540 to 660 nm. By using an optical filter on the camera, incident light is efficiently filtered yielding a better quality of raw images close to the sphere surfaces.

A high-speed camera (Ultima APX-RS, 1024 × 1024 pixels) was used to record PIV images. The camera optical axis intersected the laser-light sheet perpendicularly. Depending on the geometric configuration of collisions, a region varying from 15×15 mm^2 to 31×31 mm^2 was recorded with a spatial resolution from 33 to 68 pixel mm^{-1}. Acquisitions along the sequence were stored with a fixed frequency (400 Hz). This allows to calculate the velocity field every 2.5 ms.

The camera was synchronized with a mechanical device in order to start each sequence of images at the same position of the moving sphere. For each configuration (velocity, direction of approach, etc.) ten sequences were recorded together with a shadowgraph acquisition using an LED backlight illumination. This last one allows an accurate determination of the moving sphere position. The software used to analyze images was developed at the Institut de Mécanique des Fluides de Toulouse. The algorithm is based on a 2D FFT cross-correlation function implemented in an iterative scheme with a subpixel image deformation, according to Lecordier and Trinite [21]. The flow was analyzed by cross-correlating 50 % overlapping windows of 32×32 pixels (large gap, i.e., $e = R/3$) or 16×16 pixels (narrow gap, i.e., $e = R/10$). This yields velocity fields of 63×63, respectively 127×127, vectors. For a region size of 15×15 mm^2, this leads to a spatial resolution of 0.47 mm, respectively 0.24 mm, based on the cross-correlation window size. Each velocity field was obtained from a pair of consecutive images, which correspond to a time delay of 2.5 ms. Later, the full set of ten vector fields was averaged to provide a single mean vector field.

3 Flow Fields for Inline and Off-Centered Collisions

The first set of experiments corresponds to beads under frontal approach. This was done in Newtonian and non-Newtonian

fluids and corresponding velocity fields are presented. In a second time, an oblique approach of the beads was investigated, and then shear rate fields were compared for different shift parameters a.

3.1 Frontal Approach

In this section the drainage in the simplest configuration is presented, i.e., the frontal collision in a Newtonian fluid. In Fig. 3, dimensionless radial velocity profiles are plotted for increasing drainage Reynolds numbers from 9 to 93 (corresponding to increasing approach velocities), at the same radial position $r = 0.44R$, and for a gap e between the beads equal to $R/3$. The dimensionless representation ensures that areas under profiles are equal because mass flow rates are equal. A large dissymmetry of the profiles appears as the fluid inertia increases. This is related to the dissymmetry of the boundary conditions: a moving sphere approaches a fixed sphere.

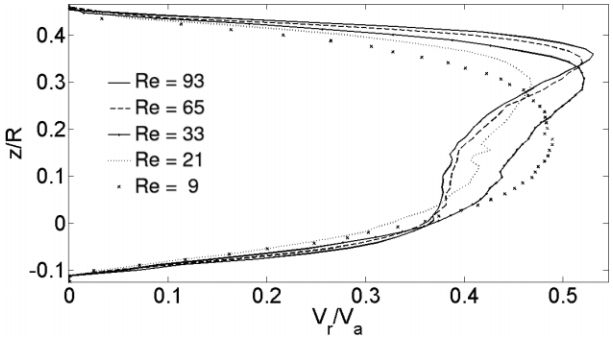

Figure 3. Radial velocity profile at $r = 0.44R$ when $e = R/3$. Frontal approach.

This profile dissymmetry is less observable in Fig. 4 corresponding to the same approach velocities and at the same radial position $r = 0.44R$ but for a smaller gap: $e = R/10$. The instantaneous Reynolds number is smaller: the fluid inertia is reduced although the maximal velocity of drainage is increased. It is important to note that experimental profiles of radial fluid velocity tend to the theoretical profile assuming pure lubrication (Re = 0) which is plotted in Fig. 4 together with experimental profiles.

The radial velocity profiles for different radial positions are presented in Figs. 5 and 6 for two gaps, respectively $e = R/3$ and $e = R/10$. They correspond to the same approach velocity V_a and present profiles for r varying from $0.1R$ to $0.44R$. Fig. 5 shows that for $e = R/3$ and Re = 33 the radial velocity profiles become more symmetric as r decreases to 0. Besides, the ejected mass flow rate (profile integral) increases with the vertical section. At a smaller gap ($e = R/10$, Fig. 6), the maximum as well as the mean radial velocity are larger at $r = 0.32R$ than for other profiles. This is consistent with the

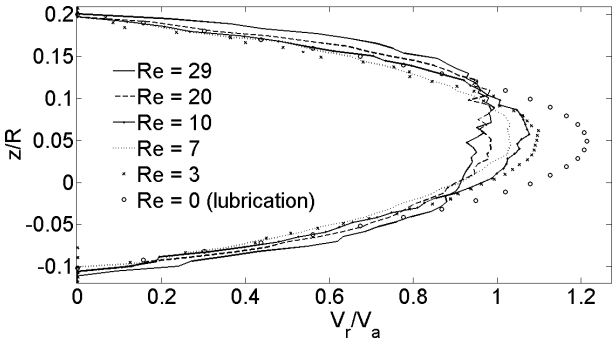

Figure 4. Radial velocity profile at $r = 0.44R$ when $e = R/10$. Frontal approach.

mass conservation criterion. A flow rate balance can be written between the mass flow pushed by the moving sphere in the z-direction and the mass flow ejected from the gap in the r-direction. Calculation of the mean velocity $\tilde{V}$ in a cylindrical section shows that the maximum for $\tilde{V}/V_a$ is obtained at $r = 0.51R$ when $e = R/3$ and at $r = 0.30R$ when $e = R/10$.

3.2 Oblique Approaches

Obviously, frontal collisions represent a very specific case. Their actual probability of occurrence is expected to be low. Indeed, it has been shown from numerical simulations of the hydrodynamics in the mill [19] that oblique collisions were the most frequent and the most intense ones. Therefore, oblique collisions for different off-centered distances aR were experimentally studied. In this configuration, the squeezing flow is no longer axisymmetric. Fluid velocities were only measured in the vertical plane crossing the spheres by their center. An oblique approach is defined by the parameter a (see Fig. 2). The velocity fields in the gap for $e = R/10$ and Re = 29 are presented in Fig. 7 for $aR = 0$, R, $1.5R$, and $2R$. The point ($r = 0$, $z = 0$) corresponds to the impact point.

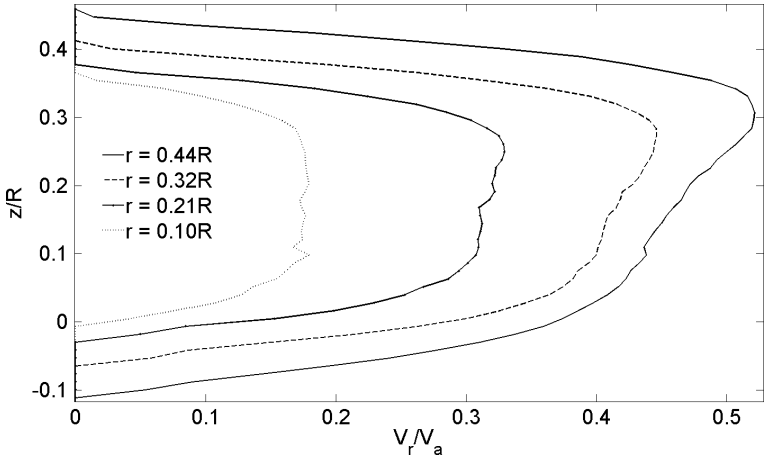

Figure 5. Radial velocity profiles for $e = R/3$ and Re = 33. Frontal approach.

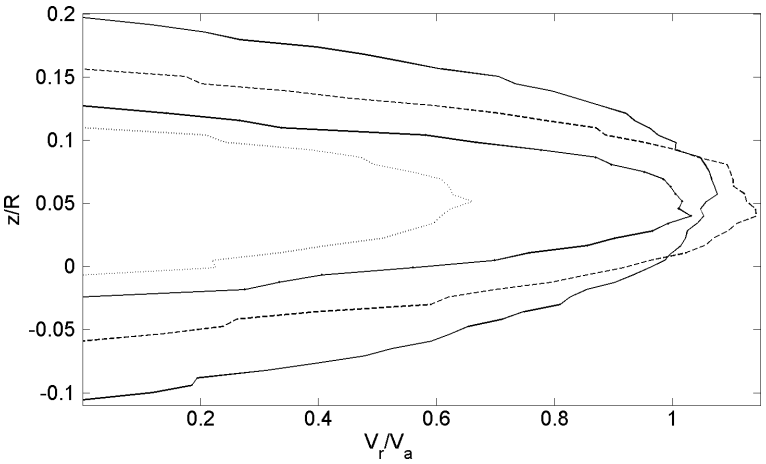

Figure 6. Radial velocity profiles for $e = R/10$ and Re = 10. Frontal approach (see legend in Fig. 5).

Comparing the cases $\alpha = 0$ (frontal approach) and $\alpha = 1$ (oblique approach), a reinforcement of the drainage for positive radial positions in the oblique case was observed. When α increases, (see $\alpha = 1.5$ and $\alpha = 2$ in Fig. 7), a modification of the drainage is observable: a counter flow appears for positive radial positions, particularly for $\alpha = 1.5$. This implies that particles of low inertia (i.e., the finest ones) may remain fixed in the gap. As a consequence, their capture probability must be higher for oblique collisions than for frontal collisions. This conclusion is common to our numerical and experimental studies.

3.3 Shear Rate Field

If the velocity field controls the feed of the efficient zone between two colliding beads, the shear rate is

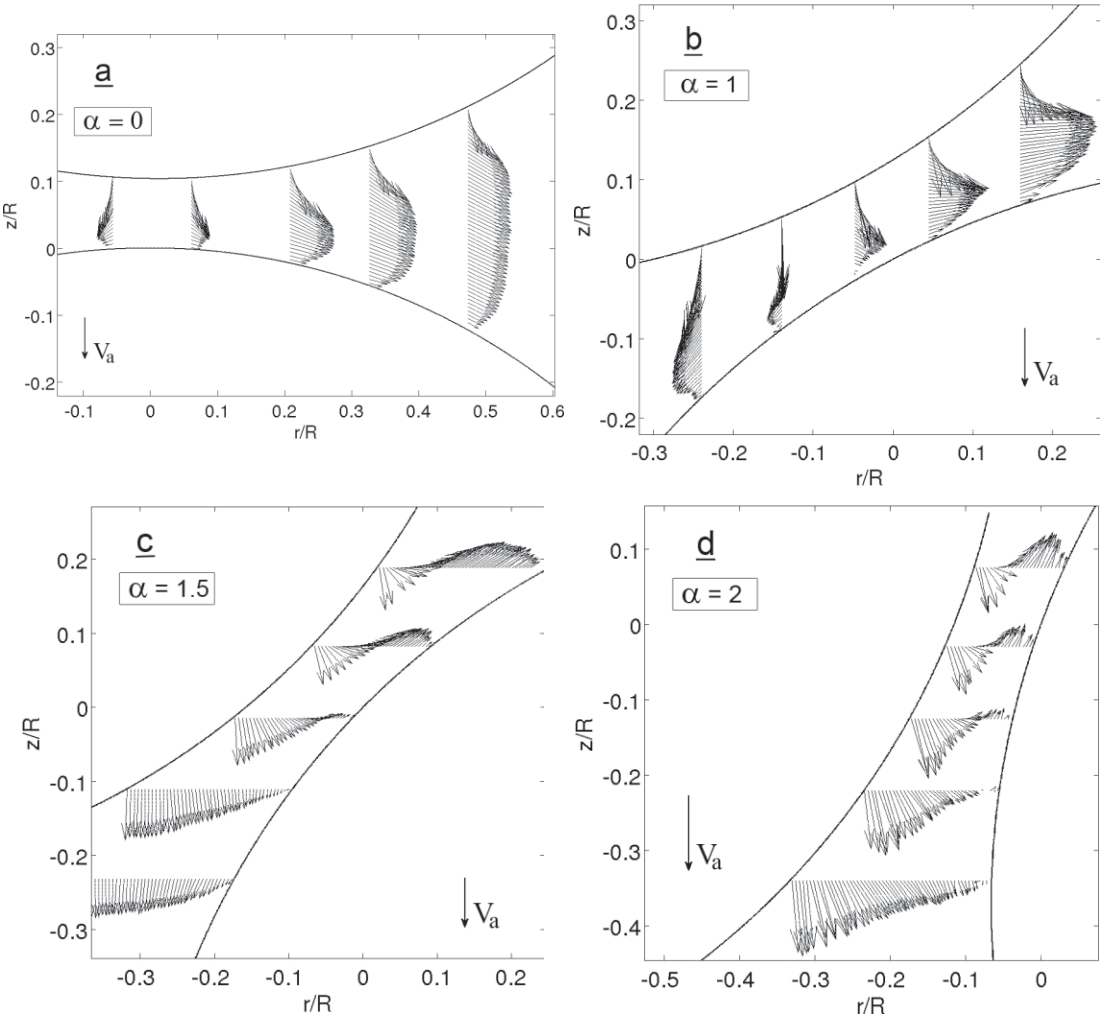

Figure 7. Velocity field in the gap between the beads ($e = R/10$, Re = 29). Frontal and oblique approach: (a) $\alpha = 0$, (b) $\alpha = 1$, (c) $\alpha = 1.5$, (d) $\alpha = 2$.

also involved in milling efficiency as it plays a role in the fragmentation process. Moreover, as suspensions in the mill may behave as a Newtonian or non-Newtonian fluid, shear rate fields are useful to describe drainage and evaluate modifications induced by non-Newtonian behavior in the gap. For axisymmetric flows, analytical expression for the shear rate $\dot{\gamma}$ reduces to:

$$\dot{\gamma} = \left[2\left(\frac{\partial V_r}{\partial r}\right)^2 + 2\left(\frac{\partial V_z}{\partial z}\right)^2 + 2\left(\frac{V_r}{r}\right)^2 + \left(\frac{\partial V_r}{\partial z} + \frac{\partial V_z}{\partial r}\right)^2 \right] \qquad (3)$$

A continuity equation for an incompressible fluid has been used to estimate terms which can not be directly measured. For an oblique collision, the validity of Eq. (3) is limited to the diametral (r, z) plane (see Fig. 2b) which is the only vertical plane of symmetry. Comparisons between the two types of collision is then restricted to this plane.

Fig. 8 shows profiles of the dimensionless shear rate $\dot{\gamma}R/V_a$ in the gap at $r = 0.44R$ for a frontal collision and for two gaps: $e = R/3$ (Fig. 8a) and $e = R/10$ (Fig. 8b), corresponding to Re = 93 and Re = 29, respectively. The two cases correspond to a same approach velocity. The shear rate is obviously maximal at the spheres' surface where velocity gradients are strong. The dissymmetry of the velocity profiles, visible at $e = R/10$ (see Fig. 5), is responsible for the dissymmetry of the shear rate profile. Besides, as for velocity profiles, the increase of the shear rate as the gap decreases is confirmed: the maximum dimensionless shear rate $\dot{\gamma}R/V_a$ reaches approximately 15 for $e = R/3$ and 40 for $e = R/10$.

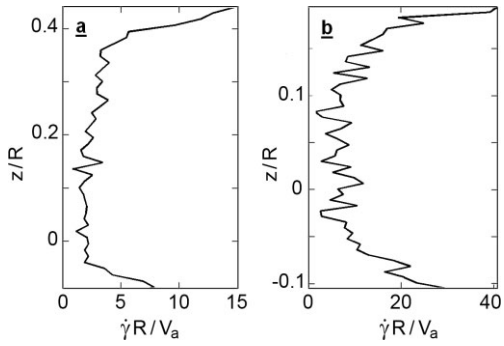

Figure 8. Dimensionless shear rate profile in the gap between the beads at $r = 0.44R$ for a given approach velocity – frontal approach: (a) $e = R/3$ (Re = 93), (b) $e = R/10$ (Re = 29).

Fig. 9 shows the evolution of the nondimensional shear rate according to the shifting distance αR for the same approach ve-

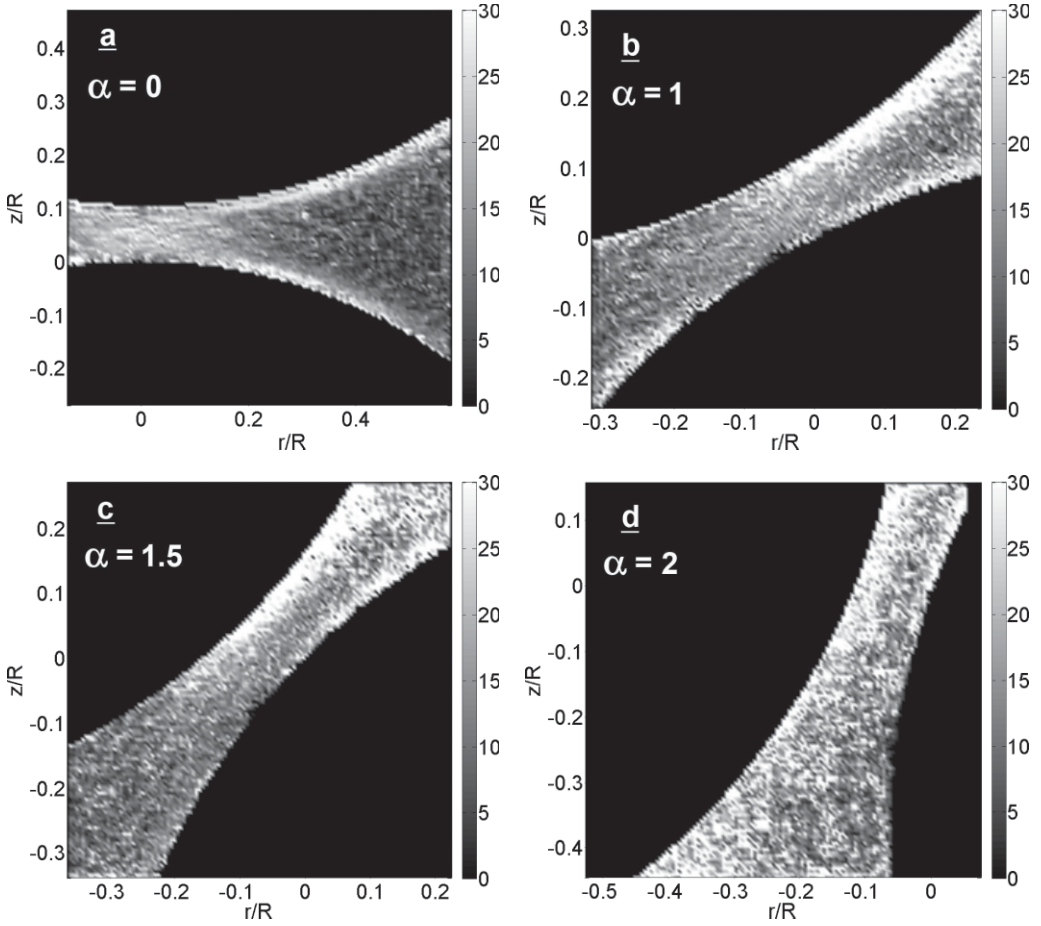

Figure 9. Shear rate field in the gap between the beads ($e = R/10$, Re = 29). Frontal and oblique approach: (a) $\alpha = 0$, (b) $\alpha = 1$, (c) $\alpha = 1.5$, (d) $\alpha = 2$.

locity and for the same gap $e = R/10$ between the spheres. As it was observed for the velocity fields, the shear rate increases with a: the regions of higher shear rate broaden from $a = 0$ to $a = 1.5$. For $a = 1.5$, it is maximal for the positive r-coordinates and the most dissymmetric because of a low intensity for the negative r-coordinates. The maximum of shear rate is about four times more intense when $a = 1.5$ compared to $a = 0$. A major influence of the fluid nature in this configuration is expected. Indeed, at a smaller gap, the fluid viscosity in the gap must significantly decrease if the suspension of particles is shear-thinning and increases if the suspension of particles is shear-thickening.

3.4 Non-Newtonian Fluids

In this large-scale experiment, the nonhydrodynamic surface interactions are neglected. However, these forces were taken into account at a macroscopic level considering suspensions with different rheological behaviors, similar to those observed in real processes [20].

The velocity field in the gap between the spheres with a shear-thinning fluid was investigated. PIV measurements were then obtained with two solutions of xanthan and for the frontal approach. The differences observed on the velocity profiles between Newtonian and non-Newtonian fluids are in the same range of the measurement accuracy, even for the smallest gap between the spheres $e = R/10$. This can be explained by the weak variation of the shear stress. Note that for a power-law index equal to 0.58 the viscosity varies over a factor of 2.6 for a decade on the shear rate. Large variations of the shear rate are then necessary to modify significantly the viscosity and influence the hydrodynamics. Because the shear stress significantly increases when the spheres approach, it is expected that non-Newtonian behavior has an influence on hydrodynamics and capture probability just before the collision.

4 Efficiency of Particle Capture

Using the instantaneous experimental velocity fields, the trajectories of fictitious particles during the spheres' approach can be computed. The focus is on determining the probability of capture in the efficient zone of milling. A particle embedded in a fluid has a trajectory governed by the force balance equation:

$$m_p \frac{D\vec{V}_p}{Dt} = \vec{F}_I + \vec{F}_D \tag{4}$$

where m_p and $\vec{V}_p$ are the mass and the velocity of the particle. In this force balance, the two dominant contributions $\vec{F}_I$ and $\vec{F}_D$ are considered, respectively, i.e., the inertia force and the drag force. In Eq. (4) the lift is neglected in view of preliminary tests and the buoyancy force has not been considered because gravity has a negligible effect on the mill scale during a collision.

The drag force is:

$$F_D = C_D \rho_f \frac{\pi D_p^2}{8} \left\| \vec{V}_f - \vec{V}_p \right\| \left(\vec{V}_f - \vec{V}_p \right) \tag{5}$$

$\vec{V}_f$ is the fluid velocity and D_p is the particle diameter. C_D is the drag coefficient of Schiller and Naumann [22]:

$$C_D = \frac{24}{Re_p} \left(1 + 0.15\, Re_p^{0.687} \right) \tag{6}$$

which is based on the particle Reynolds number:

$$Re_p = \rho_f \frac{\left\| \vec{V}_f - \vec{V}_p \right\| D_p}{\mu_f} \tag{7}$$

The effect of fluid inertia yields the force F_I:

$$F_I = m_f (1 + C_M) \frac{D\vec{V}_f}{Dt} - C_M m_f \frac{D\vec{V}_p}{Dt} \tag{8}$$

where m_f is the mass of an equivalent fluid particle and C_M is the added-mass coefficient. For spherical particles, C_M is equal to 1/2.

Conditions of similitude have to be validated also for the particles: the ratio bead to particle diameter and the Stokes number have to be equal in the milling process and in the experiment. The Stokes number of particles St is defined by Eq. (9):

$$St = \frac{1}{18} \frac{\rho_p + C_M \rho_f}{\rho_f} \frac{D_p}{D_b} Re \tag{9}$$

where the subscripts f, p, and b stand for fluid, particle, and beads, and D is the diameter. For the results presented here, particles with a diameter of 280 µm and a density of 2700 kg m^{-3} are considered: the diameter ratio D_p/D_b corresponds to the ratio observed at the end of a milling process and the density is that of calcium carbonate which was used in previous experiments [20].

Trajectory calculations are initialized by uniformly distributing particles in the gap when the distance $e = R$, corresponding to the time $t = t_1$. The time step used to solve Eq. (4) for each particle corresponds to 2.5 ms, the time between two PIV velocity fields (400 Hz being the acquisition frequency). Fig. 10 shows some trajectories of particles for different starting positions, impact velocity V_a (3.5 mm s^{-1} and 10 mm s^{-1}), and a-values of 0, 1, 1.5, and 2. The gray line corresponds to the surface of the fixed sphere. The dotted lines, parallel to the line of sphere centers when they are in contact, mark the position a particle must not overpass to be captured. A particle located at this position is in contact with the two spheres when they are in contact. The domain bounded by the dotted lines is called active volume. It clearly appears in Fig. 10 that a high impact velocity induces motion toward the fixed sphere, whatever the value a. Thus, a high velocity impact increases the capture efficiency. Following the same method, the effect of particle diameter and density has also been considered and it has been found that the increase of particle inertia increases the particle capture probability and, consequently, small particles are more easily carried by the fluid outside the active volume.

Concerning the frontal approach, starting from a defined distribution of particles in the gap at time t_1 (i.e., when the distance e is equal to R), the particles that will be present in the active volume when beads collide can be deduced, and hence, which particles will be crushed during the impact. This defines an effective volume. A capture efficiency can be evalu-

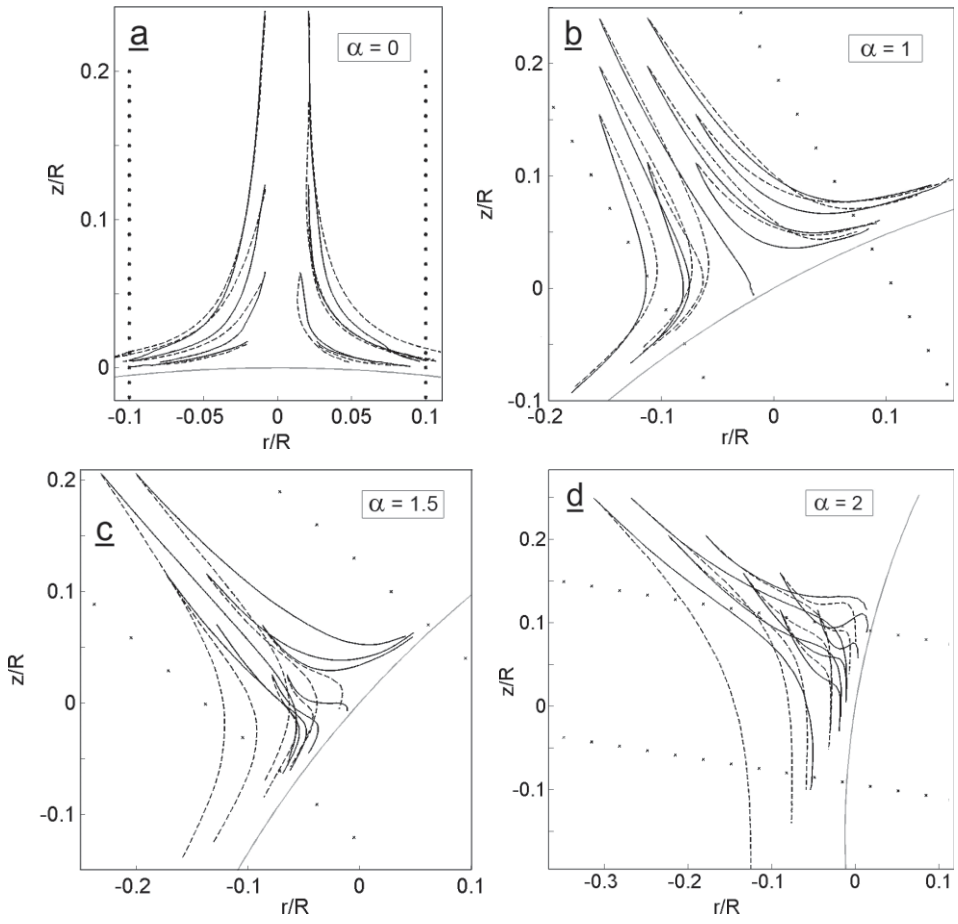

Figure 10. Particle trajectories for approach velocity V_a equal to 3.5 mm s^{-1} (dashed lines) and 10 mm s^{-1} (full lines). Frontal and oblique approach (particle diameter: 280 μm): (a) $\alpha = 0$, (b) $\alpha = 1$, (c) $\alpha = 1.5$, (d) $\alpha = 2$.

ated by comparing this volume to the active volume at t_1. The calculations done revealed that this capture efficiency slightly increases with the approach velocity but remains very weak: 1.4 % and 2.4 % for $V_a = 3.5$ mm s^{-1} and 10 mm s^{-1}, respectively. Such an estimation cannot be extended to the oblique approach since the flow is no longer axisymmetric. Nevertheless, when examining trajectories in the active volume, a monotonic behavior for small values of α is also observed: particles moving out of the active volume do not return inside. The behavior is different for large values of α (see Fig. 10d for positive z-value) where trajectories are more complex. Due to rapid variations of the flow structure in the gap during the particle approach, some particles can be observed coming back inside the active volume after having left it. This suggests that the configurations corresponding to large α-values are more efficient for milling.

4 Conclusions

A large-scale experimental device was built for investigating the fluid drainage when two grinding beads approach each other both in frontal and oblique configurations. The device and beads' dimensions as well as the experimental conditions were selected from similarity analysis on the Reynolds numbers estimated in a stirred media mill.

When the two beads are in a frontal approach, a dissymmetry of the radial velocity was observed for Reynolds numbers >10. This result can be explained since only one sphere is moving. When the beads approach each other in an oblique configuration, a modification of the drainage due to a counter flow for the larger shift distances αR and for positive radial positions was observed. This could be favorable for breakage, since particles with low inertia (i.e., the finest ones) can remain at rest in the active gap. This may increase their probability to be captured and broken. The most intense counter flow was observed for a shift distance equal to 1.5R. Concerning the shear rates, the intermediate shift distance from R to 1.5R leads to the more favorable situations for breakage.

The velocity field in the gap between the spheres was also investigated using a shear-thinning fluid. This is a simplified way of accounting for nonhydrodynamic effects in real concentrated suspensions. This showed that non-Newtonian effects are restricted in narrow regions confined around the grinding beads just before collision.

Finally, using the instantaneous experimental velocity fields, the trajectories of particles were computed. By this way, it was possible to estimate the capture probability of particles, assuming that their motion was only controlled by inertia and drag forces. This allows estimating the efficiency of impact. It was observed that the defined capture efficiency is very low and slightly increases with particle inertia, either increasing the approaching velocity or the particle size.

Acknowledgements

The authors are very grateful for the funding of the National Research Agency under the program ACI-Nanobroyage and the local support of the CNRS research federation FERMaT. They also wish to thank S. Cazin and E. Cid from the Institut de Mécanique des Fluides de Toulouse for their technical support on visualization and PIV measurements.

The authors have declared no conflict of interest.

Symbols used

C_D	[–]	drag coefficient
C_M	[–]	added-mass coefficient
D_b	[m]	bead diameter, grinding media
D_s	[m]	sphere diameter, experimental device
D_p	[m]	particle diameter
e	[m]	distance between spheres
F_D	[kg m s^{-2}]	drag force
F_I	[kg m s^{-2}]	inertia force
K	[Pa s^n]	consistency, power-law model
m_f	[kg]	mass of an equivalent fluid particle
m_p	[kg]	mass of a particle
n	[–]	power-law index, power-law model
r	[m]	radial coordinate
R	[m]	sphere radius, experimental device
Re	[–]	Reynolds number
Re_p	[–]	particle Reynolds number
St	[–]	Stokes number
$\tilde{V}$	[m s^{-1}]	mean velocity
V_a	[m s^{-1}]	approach velocity
V_f	[m s^{-1}]	fluid velocity
V_p	[m s^{-1}]	particle velocity
V_r	[m s^{-1}]	radial velocity
V_z	[m s^{-1}]	axial velocity

Greek symbols

α	[–]	shift parameter (off-centered approach)
ΔU	[m s^{-1}]	maximum relative velocity between grinding beads (mill apparatus)
$\dot{\gamma}$	[s^{-1}]	shear rate
μ_f	[kg m^{-1} s^{-1}]	dynamic viscosity, fluid for experiments
ν_s	[m^2 s^{-1}]	kinematic viscosity, suspension to be ground
ν_f	[m^2 s^{-1}]	kinematic viscosity, fluid for experiments
ρ_f	[kg m^{-3}]	fluid density
ρ_p	[kg m^{-3}]	particle density

References

[1] S. Mende, F. Stenger, W. Peukert, J. Schwedes, *Powder Technol.* **2003**, *132 (1)*, 64.
[2] F. Stenger, S. Mende, J. Schwedes, W. Peukert, *Powder Technol.* **2005**, *156 (2–3)*, 103.
[3] F. Stenger, S. Mende, J. Schwedes, W. Peukert, *Chem. Eng. Sci.* **2005**, *60 (16)*, 4557.
[4] C. Knieke, M. Sommer, W. Peukert, *Powder Technol.* **2009**, *195 (1)*, 25.
[5] L. Blecher, A. Kwade, J. Schwedes, *Powder Technol.* **1996**, *86 (1)*, 59.
[6] G. L. Lane, *2nd Int. Conference on CFD in the Minerals and Process Industries CSIRO,* Melbourne, Australia, December **1999**.
[7] H. Mori, H. Mio, J. Kano, F. Saito, *Powder Technol.* **2004**, *143–144*, 230.
[8] D. Gudin, J. Kano, F. Saito, *Adv. Powder Technol.* **2007**, *18 (5)*, 555.
[9] R. Y. Yang, C. T. Jayasundara, A. B. Yu, D. Curry, *Miner. Eng.* **2006**, *19 (10)*, 984.
[10] C. T. Jayasundara et al., *Min. Eng.* **2009**, *22 (11)*, 886.
[11] J. Theuerkauf, J. Schwedes, *Powder Technol.* **1999**, *105 (1–3)*, 406.
[12] J. Theuerkauf, J. Schwedes, *Chem. Eng. Technol.* **2000**, *23 (3)*, 203.
[13] A. Kwade, *Powder Technol.* **1999**, *105 (1–3)*, 382.
[14] G. Mende, *Ph.D. Thesis*, Technical University Braunschweig, Germany **2005**.
[15] J. Zhang et al., *Powder Technol.* **1999**, *106 (1–2)*, 98.
[16] G. G. Joseph, R. Zenit, M. L. Hunt, A. M. Rosenwinkel, *J. Fluid Mech.* **2001**, *433*, 429.
[17] P. Gondret, M. Lance, L. Petit, *Phys. Fluids* **2002**, *14 (2)*, 643.
[18] R. H. Davis, D. A. Rager, B. T. Good, *J. Fluid Mech.* **2002**, *468*, 107.
[19] R. Gers et al., *Chem. Eng. Sci.* **2010**, *65 (6)*, 2052.
[20] C. Frances, D. Anne-Archard, in *Proc. of the 4th Colloque Science et Technologie des Poudres*, *Récents progrès en Génie des Procédés no. 91* (Ed: P. Guigon), Lavoisier, Paris **2004**.
[21] B. Lecordier, M. Trinite, *PIV03 Symposium*, Busan, Korea **2003**.
[22] L. Schiller, A. Naumann, *Z. Ver. Dtsch. Ing.* **1933**, *77*, 138.

